RESEARCH ARTICLE

NEUROSCIENCE

Lifespan Mapping of EEG Source Spectral Dynamics with $\xi - \alpha$NET

Ronaldo Garcia Reyes[1,2,*,†], Ariosky Areaces Gonzales[1], Ying Wang[1], Yu Jin[1], Ludovico Minatti[1,3] and Pedro A. Valdes–Sosa[1,2,*,†]

ABSTRACT

We formulate a new class of parametric, multivariate, and structurally informed spectral components model of the EEG, the $\xi - \alpha$NET, that allows us to map the Lifespan of EEG source spectral dynamics across a large data set of EEG cross spectrum at high spatial resolution. This approach accurately estimates source spectral components and effective connectivity through the use of biophysical modeling while maintaining computational efficiency, as confirmed by simulation benchmarks. We are able to analyze source dynamics with a resolution of 8,003 voxels from the HarMNqEEG dataset, which includes scalp EEG cross-spectrum tensors collected from 1965 subjects across 9 countries, using various devices and accounting for different age groups. Our findings indicate that the Bayesian Model Inversion of the $\xi - \alpha$NET allows to map Lifespan of conduction delays that follows a U-shaped trajectory, which contrasts with independently recorded myelin concentration measurements. Moreover, we assess the spatiotemporal distribution of spectral components, revealing that the aperiodic or fractal component has an isotropic spatial distribution on the cortical surface. While the generator's spectral peak in the α band, i.e., α-rythms, is localized on the visual areas of the brain. Using a Zero Inflated Gaussian model, our findings indicate that the mode frequency that characterizes the α-rythms or Peak Alpha Frequency shows an inverted U-shaped trajectory for both hemispheres across the Lifespan and a spatial gradient of zero inflation in PAF across the cortex that flattens the trajectory from posterior to frontal areas. We provide both the code of the $\xi - \alpha$NET and the source solution of the spectral dynamics for the HarMNqEEG.

Keywords: Lifespan, Spectral Components, EEG-Dataset, Conduction Delays, Source Analysis, Alpha-Rythms

[1] Clinical Hospital of Chengdu Brain Science Institute, University of Electronic Science and Technology of China, 610054, Chengdu, China;
[2] Neuroinformatics, Cuban Neurosciences Center, 11300, Havana, Cuba;
[3] Center for Mind/Brain Science (CIMeC), University of Trento, 38123, Trento, Italy

[*]**Corresponding authors.** Email: gaussn0ise29@gmail.com pedro.valdes@neuroinformatics-collaboratory.org. [†]Equally contributed to this work..

Received: XX XX Year;
Revised: XX XX Year;
Accepted: XX XX Year

INTRODUCTION

Neural oscillations underlie both brain function and dysfunction [1,2]. These oscillations manifest in EEG power spectra as Spectral Components (SC) with distinct spatial and frequency-domain signatures [3–7]. Two main SC typically emerge: an Aperiodic Component (AC), referred to as the Xi-process (ξ) and characterized by a $1/f$ decay, and a Periodic Component (PC) with a dominant spectral peak in the alpha band (7–13 Hz), known as the Alpha-process (α) [3,4,8,9]. Modeling and fitting SC has a long tradition, broadly classified into univariate or multivariate approaches depending on whether they target the EEG spectrum or cross-spectrum, respectively.

Pioneering work by Zetterberg et al. [10] introduced an early univariate parametric model of EEG signals, representing them via a stationary discrete-time random process governed by a linear difference equation. Building on this foundation, Pascual et al. [8] proposed the $\xi - \alpha$ model, the first parametric framework to use additive mixing of two independent SC (the ξ- and α-processes) for explaining EEG power spectra. This model uses a Student's t distribution to fit SC on the natural scale. Amador et al. [11] subsequently demonstrated the $\xi - \alpha$ model utility for characterizing EEG maturation by deriving developmental equations that captured age-related changes in the average EEG power spectrum. Several other univariate parametric models have since appeared, many relying on multiplicative mixing of SC. BOSC (Better OSCillation detection) applies a chi-squared test to detect

PC, assuming a $1/f$ form for the AC in log-log space [12]. IRASA (Irregular Resampling Auto Spectral Analysis) separates fractal and periodic activities by exploiting their differing robustness to resampling but cannot isolate distinct spectral peaks [13]. FOOOF (Fitting Oscillations & One Over F) employs power-law and Gaussian functions to fit AC and PC, respectively, in log scale [9], and SPRiNT (Spectral Parameterization Resolved in Time) [14] extends this approach to time-resolved spectral decomposition. PAPTO (Periodic / Aperiodic Parametrization of Transient Oscillations) models spectral peaks arising from transient oscillatory events [15]. Relaxing strict parametric assumptions, Hu et al. [16] introduced the $\xi-\pi$ model, a non-parametric SCM with additive mixing of SC. However, it lacks a full multivariate formulation and does not incorporate structural data.

The first multivariate SCM, the Multivariate $\xi-\alpha$ model, was introduced by Pascual et al. [8], extending the univariate $\xi-\alpha$ framework to scalp EEG signals by positing that the observed cross-spectrum arises from a linear superposition of ξ and α cross-spectra. However, this initial approach was limited to artifact-prone scalp EEG. Valdes-Sosa et al. [17] later addressed volume conduction effects by developing a source-space $\xi-\alpha$ model that treats the AC component as a short-range isotropic process on the cortical surface. While this represented a significant advance by attributing activity to cortical origins, it did not yet leverage structural data to shape the spatial distribution of SC. More recently, Pascual et al. [18] introduced a Cortical $\xi-\alpha$ model that further generalizes the traditional $\xi-\alpha$ model to encompass whole-cortex activity spectra and intracortical functional connectivity of ξ and α processes.

SCM has broad applications in neuroscience for studying brain development, cognitive performance, and psychiatric conditions or to inform biophysical models for brain simulation [19,20]. Nonetheless, several key challenges persist. Standard SC analysis usually involves two steps: (1) estimating the scalp or source-level EEG spectrum (using inverse methods such as eLORETA, LCMV, or VARETA) and (2) fitting an SCM to these estimates. This purely data-driven approach overlooks structural information (e.g., anatomical connectivity, tract lengths, and conduction delays), even though these factors strongly shape the spatiotemporal distribution of SC by influencing coherence and phase [21–23]. Moreover, source-level approaches are computationally expensive, as the number of parameters scales quadratically with the number of voxels and linearly with the number of frequencies. Consequently, most spatiotemporal SC analyses use only low-resolution data from relatively small samples, limiting statistical power. The lack of computationally efficient models that fully incorporate structural information hampers large-scale normative studies intended to characterize typical developmental trajectories [24].

To address these limitations, a very promising approach is carrying out detailed modeling as in the Digital Twin Brain, which simulates the neural activity of 86 billion neurons and around 100 trillion connection parameters [19,25–28]. Due to the limited resolution of in-vivio measurements used in clinical practice, we opted for a macroscopic approach instead by introducing the $\xi-\alpha$NET, a parametric multivariate SCM that integrates structural data and biophysical modeling within a single generative framework. Drawing on the original $\xi-\alpha$ model, $\xi-\alpha$NET simultaneously estimates source-level SC and effective connectivity, encoded by parameters that scale linearly with the number of voxels. By retaining both accuracy and computational efficiency, $\xi-\alpha$NET enables high-resolution analyses of extensive EEG datasets, including HarMNqEEG, which features EEG cross-spectrum tensors from 1965 subjects across nine countries, multiple devices, and different age groups [24]. This advance makes it feasible to map source-level EEG spectral dynamics over the Lifespan, establish the spatiotemporal distribution of SC, and quantify conduction delays with high statistical power—outcomes vital for future normative studies and precision neural field simulations.

RESULTS

$\xi-\alpha$NET

Foward Model

We aim to develop a mesoscale generative model of cortical activity ($\xi-\alpha$NET) that incorporates structural information, conduction delays, spectral components, and sparse priors to account for the observed EEG in sensor space ($\mathbf{v}_t \in \mathbb{R}^{N_c \times 1}$). To achieve this, we propose that each cortical generator corresponds to a thalamocortical unit, where the activity is a linear superposition of two independent spectral processes: the $\xi-\alpha$ process, which corresponds to the aperiodic component ($\mathbf{j}_t^{\xi} \in \mathbb{R}^{N_v \times 1}$), and the α spectral peak, which represents the oscillatory component ($\mathbf{j}_t^{\alpha} \in \mathbb{R}^{N_v \times 1}$) of the EEG spectra. Each spectral component is embedded

within a linear autoregressive network, or a multivariate vector autoregressive (MVAR) model, where the spatio-temporal correlations between generators ($\mathbf{A}_\tau$) are shaped by anatomical connectivity ($\mathbf{C} \in \mathbb{R}^{N_v \times N_v}$) and conduction delays ($\mathbf{D} \in \mathbb{R}^{N_v \times N_v}$). The model's innovation ($\mathbf{n}_t^\xi$ and $\mathbf{n}_t^\alpha \in \mathbb{R}^{N_v \times 1}$) processes further define the spectral distribution of each component. Using matrix notation, the observation and state-space equations of the generative model of the cortical activity are:

$$
\begin{aligned}
&\mathbf{v}_t = \mathbf{K}\mathbf{j}_t + \mathbf{n}_t^v, \\
&\mathbf{j}_t = \mathbf{j}_t^\xi + \mathbf{j}_t^\alpha. \\
&\mathbf{j}_t^\xi = \sum_{\tau>0} \mathbf{A}_\tau \mathbf{j}_{t-\tau}^\xi + \mathbf{n}_t^\xi, \\
&\mathbf{j}_t^\alpha = \sum_{\tau>0} \mathbf{A}_\tau \mathbf{j}_{t-\tau}^\alpha + \mathbf{n}_t^\alpha. \\
&\mathbf{A}_\tau = \mathbf{W}_C \odot \mathbf{C} \odot \delta\big(\tau - \mathbf{W}_D \odot \mathbf{D}\big), \\
&\mathbf{n}_t^v \sim \mathcal{N}(0, \mathrm{diag}(\boldsymbol{\sigma}_t)), \quad \boldsymbol{\sigma}_t = \mathcal{F}^{-1}[\boldsymbol{\sigma}_\omega], \\
&\mathbf{n}_t^\xi \sim \mathcal{N}(0, \mathrm{diag}(\boldsymbol{\xi}_t)), \quad \boldsymbol{\xi}_t = \mathcal{F}^{-1}[\boldsymbol{\xi}_\omega], \\
&\mathbf{n}_t^\alpha \sim \mathcal{N}(0, \mathrm{diag}(\boldsymbol{\alpha}_t)), \quad \boldsymbol{\alpha}_t = \mathcal{F}^{-1}[\boldsymbol{\alpha}_\omega], \\
&\boldsymbol{\xi}_\omega = t\big(\omega \mid \mathbf{e}\big), \quad \boldsymbol{\alpha}_\omega = t\big(\omega \mid \mathbf{a}\big), \\
&\mathbf{e} \sim \exp(||\mathbf{e}||_{1,1} \mid \lambda_2),\ \mathbf{a} \sim \exp(||\mathbf{a}||_{1,1} \mid \lambda_3), \\
&\boldsymbol{\sigma}_\omega \sim \exp\big(||\boldsymbol{\sigma}_\omega||_2^2 \mid \lambda_1\big),
\end{aligned}
\tag{1}
$$

where $\mathbf{K} \in \mathbb{R}^{N_c \times N_v}$ is the normal lead-field matrix that maps source activity to sensor-level EEG measurements, and $\odot$ denotes the Hadamard element-wise product. The parameter τ represents a conduction delay, while $\mathbf{W}_C \in \mathbb{R}^{N_v \times N_v}$ and $\mathbf{W}_D \in \mathbb{R}^{N_v \times N_v}$ are unknown weight matrices modulating the baseline anatomical connectivity and conduction delays, respectively. The function δ denotes the Dirac delta function, and $\mathrm{diag}(\cdot)$ represents the diagonalization operator. The symbol $\mathcal{F}^{-1}$ corresponds to the inverse Fourier transform. The spectral components are parameterized by the vectors $\boldsymbol{\xi}_\omega \in \mathbb{R}^{N_v \times 1}$ and $\boldsymbol{\alpha}_\omega \in \mathbb{R}^{N_v \times 1}$, which describe the spectral mapping across frequencies using a Student's t-distribution: $t(\omega \mid a, b, c, d) = a/\big(1 + b(\omega - d)^2\big)^c$ [8,17,18]. These spectral components are determined by the parameters $\mathbf{e} \in \mathbb{R}^{N_v \times 3}$ and $\mathbf{a} \in \mathbb{R}^{N_v \times 4}$, represented as matrices. To enforce sparsity in the cortical distribution of spectral components, we impose Group Lasso priors [29], where each row of these matrices defines a group within the Group Lasso framework. This ensures that if a particular cortical region exhibits zero power in its spectral components, all corresponding spectral parameters in that region are also set to zero, promoting sparse solutions. To achieve this, we employ an exponential prior $\exp(\cdot|\cdot)$ where the matrix $L^{1,1}$ norm, defined as:$||U||_{1,1} = \sum_{i=1}^{N} ||U_{i,:}||_1$ and the λ's are the regularization hyperparameters .

Table 1. Summary of model components

Parameter	Interpretation
$W_C \in \mathbb{R}^{N_v \times N_v}$	Anatomic Connectivity Weight
$W_D \in \mathbb{R}^{N_v \times N_v}$	Conduction Delay Weight
$\boldsymbol{\sigma}_\omega \in \mathbb{R}^{N_c \times 1}$	Sensor Noise
$\mathbf{e}_{:,1} \in \mathbb{R}^{N_v \times 1}$	ξ-Power (dB)
$\mathbf{e}_{:,2} \in \mathbb{R}^{N_v \times 1}$	ξ-Width (sec)
$\mathbf{e}_{:,3} \in \mathbb{R}^{N_v \times 1}$	ξ-Decay Exponent
$\mathbf{a}_{:,1} \in \mathbb{R}^{N_v \times 1}$	α-Power (dB)
$\mathbf{a}_{:,2} \in \mathbb{R}^{N_v \times 1}$	α-Width (sec)
$\mathbf{a}_{:,3} \in \mathbb{R}^{N_v \times 1}$	α-Decay Exponent
$\mathbf{a}_{:,4} \in \mathbb{R}^{N_v \times 1}$	Peak Alpha Frequency (Hz)

Note: N_v is the number of voxels and N_c is the number of channels. The notation $\mathbf{Y}_{:,k}$ refers to the k-th column of the matrix $\mathbf{Y}$).

The forward model parameters are divided into two categories. The first category includes the SC parameters $\mathbf{x} = \big(\mathrm{vec}_r(\mathbf{e})^\top, \mathrm{vec}_r(\mathbf{a})^\top, \boldsymbol{\sigma}^\top\big)^\top \in \mathbb{R}^{7N_v + N_\omega}$, which encode information about the spectral processes (vec_r its the row-wise vectorization operator). The second category comprises the structural modulation parameters $\mathbf{w} = \big(\mathrm{vec}_r(\mathbf{W}_C)^\top, \mathrm{vec}_r(\mathbf{W}_D)^\top\big)^\top \in \mathbb{R}^{2N_v^2}$, which modulate the structural connectivity and conduction delays. While $\boldsymbol{\lambda} = (\lambda_1, \lambda_2, \lambda_3)^\top$ are the hyperparameters of the model that only regularize the SC sparsity.

Bayesian Model Inversion

Our goal is to estimate the free parameters of the $\xi - \alpha$NET model [Tab. 1] from the observed EEG cross-spectra data. We do this using a Bayesian framework, where parameter estimation is framed as a MAP problem, combining the negative log-likelihood of the data and prior regularization terms. The optimization problem is defined as (see Supplementary Materials A):

$$
\begin{aligned}
&\left(\mathbf{x}^{(j)}, \mathbf{w}^{(j)}\right) = \arg\min_{\mathbf{x},\mathbf{w}>0} F\left(\mathbf{S}^{(j)} \mid \mathbf{x}, \mathbf{w}\right), \\
&F\left(\mathbf{S}^{(j)} \mid \mathbf{x}, \mathbf{w}\right) = f + g, \\
&f = \sum_\omega \left(-\log|\boldsymbol{\Omega}_\omega| + \mathrm{tr}\left(\mathbf{S}_\omega^{(j)} \boldsymbol{\Omega}_\omega\right)\right), \\
&g = \lambda_1 \|\boldsymbol{\sigma}\|_2^2 + \lambda_2 \|\mathbf{e}\|_{1,1} + \lambda_3 \|\mathbf{a}\|_{1,1}, \\
&\boldsymbol{\Omega}_\omega = \left(\sigma_\omega \mathbf{I}_{N_c} + \mathbf{T}_\omega \mathrm{diag}\left(\boldsymbol{\xi}_\omega + \boldsymbol{\alpha}_\omega\right) \mathbf{T}_\omega^\dagger\right)^{-1}, \\
&\mathbf{T}_\omega = \mathbf{K}\left(\mathbf{I}_{N_v} - \mathbf{W}_C \odot \mathbf{C} \odot \exp\left(-2\pi i \omega \mathbf{W}_D \odot \mathbf{D}\right)\right)^{-1},
\end{aligned}
\tag{2}
$$

where $\mathbf{S}^{(j)} \in \mathbb{R}^{N_c \times N_c \times N_w}$ it the observed

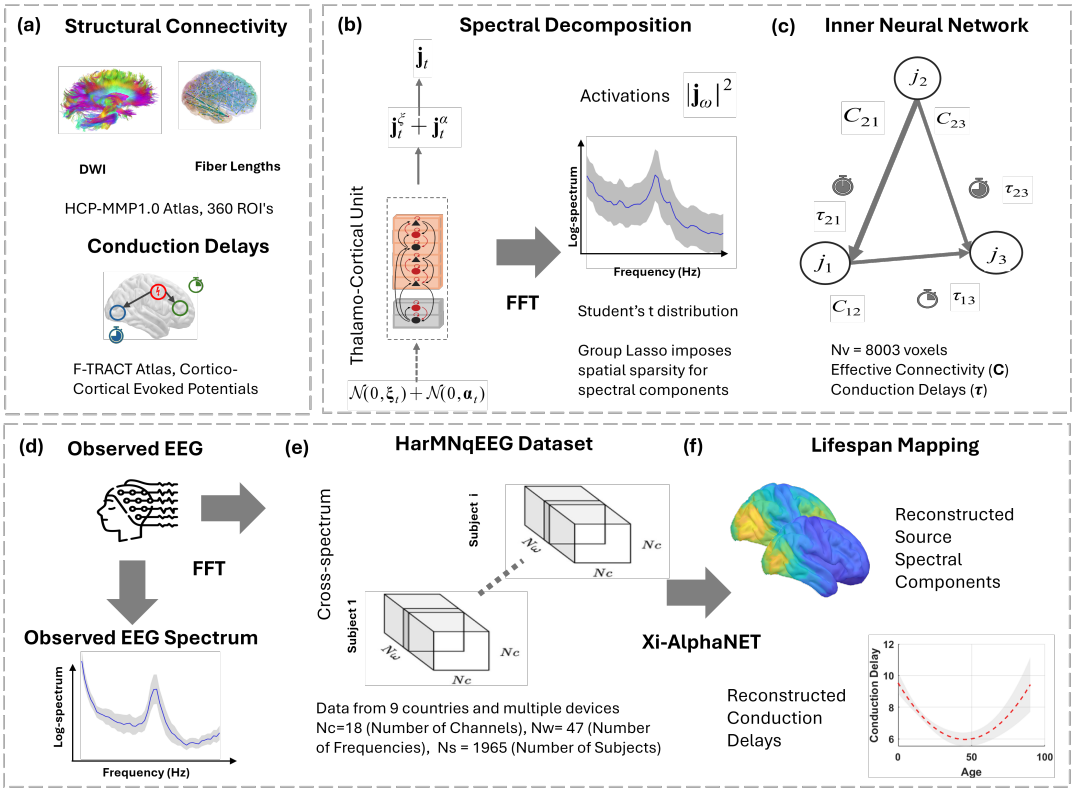

Figure 1. The $\xi - \alpha$NET forward and inverse model. **(a)** The $\xi - \alpha$NET is constructed using structural data, specifically structural connectivity obtained using Diffusion Tensor Imaging (DTI) and Conduction delays obtained using Cortico Cortical Evoked Potentials. **(b)** Neurons within a voxel are organized into a micro thalamocortical unit. Each spectral process in this unit represents endogenous Gaussian innovations, which produce the source activation ($\mathbf{j}_t$). As a result, the spectrum of the activation ($|\mathbf{j}_\omega|^2$) exhibits distinct spectral components. **(c)** The spatiotemporal dynamics of a network of thalamocortical units (j_i) adhere to an autoregressive model in which conduction delays ($\boldsymbol{\tau}$) and structural connectivity ($\mathbf{C}$) influence spatiotemporal correlation. **(d)** At the scalp level, the $\xi - \alpha$NET generates an EEG signal containing various spectral components. **(e)** Using this model, we analyze source dynamics with a resolution of 8,003 voxels from the HarMNqEEG dataset. This dataset includes scalp EEG cross-spectrum tensors collected from 1,965 subjects across nine countries, utilizing various devices and accounting for different age groups. **(f)** This approach enables the mapping of the Lifespan of spectral components and conduction delays in the source space.

scalp cross-spectrum of the subject j. The first term, f, represents the negative log-likelihood of the observed spectrum which is a smooth and nonconvex function with gradient respect to the spectral components:

$$\begin{aligned}
\frac{\partial f}{\partial \mathbf{e}_{ik}} &= \sum_{\omega} \left(\mathbf{T}_{\omega}^{\dagger} \boldsymbol{\Omega}_{\omega} \left(\mathbf{I}_{N_c} - \mathbf{S}_{\omega}^{(j)} \boldsymbol{\Omega}_{\omega} \right) \mathbf{T}_{\omega} \right)_{ii} \frac{\partial \xi_{\omega,i}}{\partial \mathbf{e}_{ik}}, \\
\frac{\partial f}{\partial \mathbf{a}_{ik}} &= \sum_{\omega} \left(\mathbf{T}_{\omega}^{\dagger} \boldsymbol{\Omega}_{\omega} \left(\mathbf{I}_{N_c} - \mathbf{S}_{\omega}^{(j)} \boldsymbol{\Omega}_{\omega} \right) \mathbf{T}_{\omega} \right)_{ii} \frac{\partial \boldsymbol{\alpha}_{\omega,i}}{\partial \mathbf{a}_{ik}}, \\
\partial_{\sigma_\omega} f &= \operatorname{tr} \left(\boldsymbol{\Omega}_{\omega} \left(\mathbf{I}_{N_c} - \mathbf{S}_{\omega}^{(j)} \boldsymbol{\Omega}_{\omega} \right) \right).
\end{aligned} \tag{3}$$

Here, the precision matrix $\boldsymbol{\Omega}_\omega$ is a function of the structural and spectral parameters. The propagation operator $\mathbf{T}_\omega$ incorporates the structural connectivity and conduction delays. Additionally, the second term, g, encodes the regularization imposed by the priors on the spectral components (negative log prior,) which is a nonsmooth convex function.

Due to the nature of the optimization problem in Eqs. (2), there are multiple potential local minima. To address this, we used a two-step approach with profile likelihood methods. First, we estimated the structural modulation parameters ($\mathbf{w} = (w_D, w_C)$), treating the delay and connectivity weights as scalars to simplify the problem. Then, we applied Bayesian optimization to explore the parameter space, guided by prior knowledge of lifespan delay variations (Lemarechal et al., [30]), which helped define a plausible physiological search region. For SC parameter estimation ($\mathbf{x}$), we used Stochastic-FISTA (Fast Iterative Shrinkage-Thresholding Algorithm) with random initialization, using 50 uniform random initializations within the search space. Hyperparameters were selected through Bayesian optimization, minimizing the Bayesian Information Criterion (BIC) of the likelihood function, with degrees of freedom determined by the number of nonzero elements in $\mathbf{x}$. The hyperparameter search space was estimated for each subject, ensuring that the optimization problem

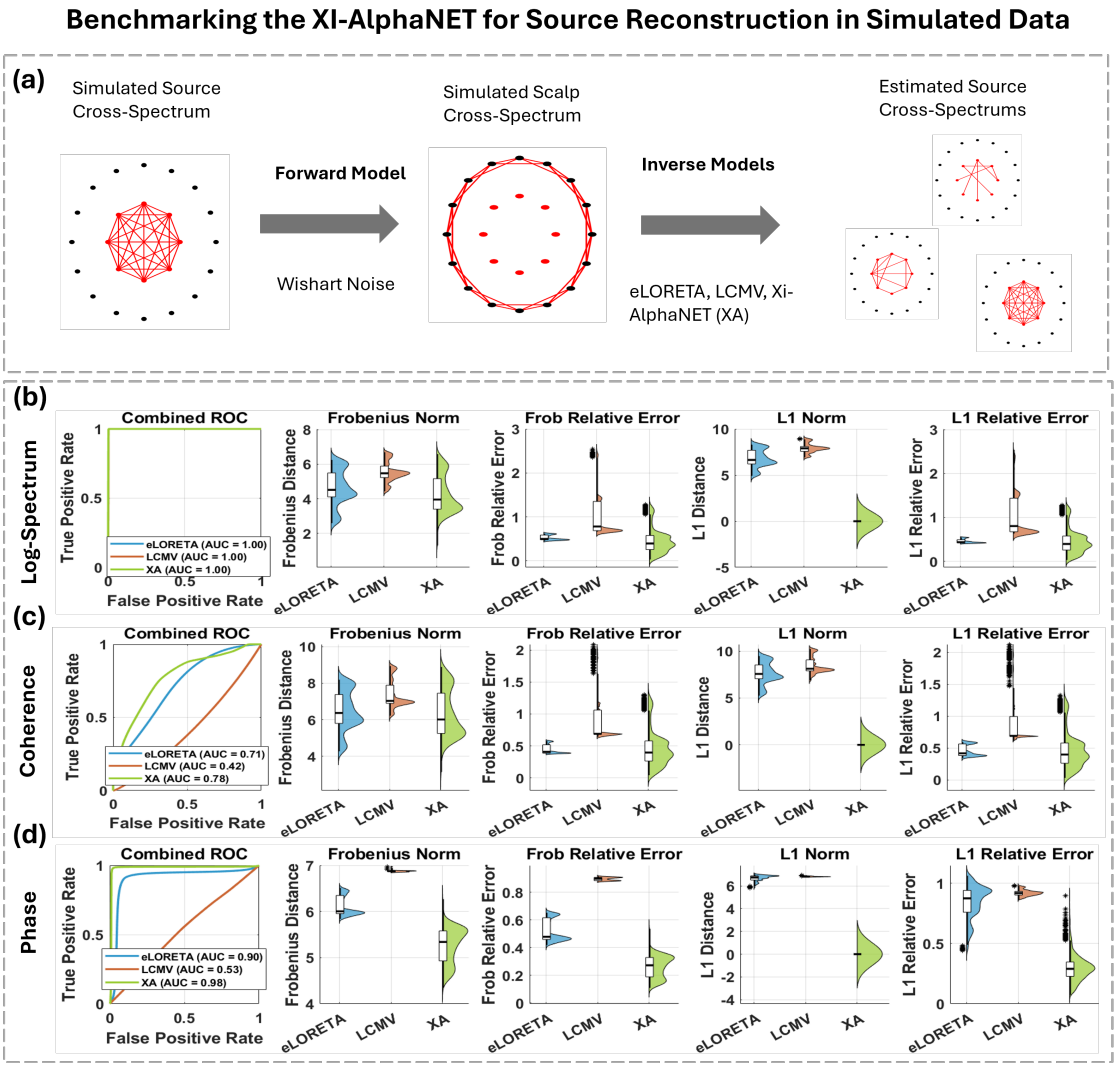

Figure 2. Validation of the $\xi - \alpha$NET Model. (**a**) Illustrates the methodology used for conducting the simulations (Nsim = 100). First, we simulate the Source Cross-Spectrum and, using a forward model, obtain the simulated Scalp Cross-Spectrum. Then, we estimate the corresponding Source Cross-Spectrum with various inverse solution methods. (**b**) Shows the performance of inverse solution methods in estimating the Log-Spectrum, evaluated using different scores. (**c**) Displays the performance of the methods in estimating the Coherence matrix (absolute value) derived from the Cross-Spectrum. (**d**) Highlights the performance of the methods in estimating the Coherence matrix (phase value) from the Cross-Spectrum. We use ROC analysis to validate the classification of active connectivity or activation and Frobenius and L1 distances to measure similarity in smoothness and sparsity. The results show that both eLORETA and $\xi - \alpha$NET perform similarly in estimating the Log-Spectrum and Coherence (absolute value), while $\xi - \alpha$NET outperforms in phase estimation.

does not lead to trivial SC solutions (see Supplementary Materials B).

Benchmarking the $\xi - \alpha$NET for Source Reconstruction in Simulated Data

The $\xi - \alpha$NET Bayesian inversion yields the estimated source cross-spectrum as:

$$\mathbf{\Sigma}_\omega = \mathbf{\Gamma}_\omega \text{diag}\left(\boldsymbol{\xi}_\omega + \boldsymbol{\alpha}_\omega\right) \mathbf{\Gamma}_\omega^\dagger,$$

$$\mathbf{\Gamma}_\omega = \left(\mathbf{I}_{N_v} - \mathbf{W}_C \odot \mathbf{C} \odot \exp\left(-2\pi i \omega \mathbf{W}_D \odot \mathbf{D}\right)\right)^{-1},$$

we then benchmark the performance of the $\xi - \alpha$NET model for source reconstruction against two established inverse solution methods: eLORETA and LCMV [31,32]. We limit our simulations to source reconstruction in the ROI space ($Nr = 360$).

The simulation began by generating a source cross-spectrum. We randomly selected 100 subjects from the HarMNqEEG dataset and computed the mean source cross-spectrum using Minimum Norm Estimation (MNE) [33]. Wishart noise was then added to introduce variability. This simulated source cross-spectrum was projected onto the scalp using the MNE forward operator to create a corresponding simulated scalp cross-spectrum. The simulated scalp cross-spectrum was subsequently used as in-

put for the three inverse methods—eLORETA, LCMV, and $\xi - \alpha$NET—to estimate the source cross-spectrums [Fig. 2(a)]. The performance of the models was assessed using five metrics: ROC analysis, Which evaluates the ability to identify active sources or connections. Frobenius norm and Frobenius relative norm: Measure the overall distance between the true and estimated source cross-spectrum. L_1 norm and L_1 relative norm: Assess the sparsity and structural accuracy of the reconstructed cross-spectrum.

For the reconstruction of the log-spectrum (diagonal of the cross-spectrum), the $\xi - \alpha$NET model generally outperformed eLORETA and LCMV in terms of the L_1 distance and classification accuracy of active voxels (ROC curves). However, the violin plots for the Frobenius relative norm and L_1 relative norm reveal that eLORETA had a lower variance in its performance compared to $\xi - \alpha$NET and LCMV. This indicates that eLORETA's estimates were more stable and consistent across the 100 simulations, even if its median error was higher than $\xi - \alpha$NET's. The reduced variance suggests that eLORETA might be less sensitive to variations in the simulated data, which could make it a more predictable method in scenarios where stability is critical [Fig. 2(b)].

A similar pattern emerges for coherence matrix (absolute value of the crosspectrum) reconstruction. $\xi - \alpha$NET outperformed eLORETA and LCMV in terms of absolute accuracy, as reflected in lower L_1 and Frobenius norms, and the ROC curves show slightly better classification performance for active connections. However, eLORETA again exhibited less variance in the Frobenius relative norm and L_1 relative norm, as shown by the narrower violin plots. This stability may indicate that eLORETA relies on more robust underlying assumptions, leading to consistent performance, though at the expense of reduced accuracy for sparse structures like those in the coherence matrix [Fig. 2(c)].

In the reconstruction of the phase of the cross-spectrum, $\xi - \alpha$NET demonstrated significant advantages across all metrics, outperforming both eLORETA and LCMV by a substantial margin. Unlike in the log-spectrum and coherence reconstruction, eLORETA's stability was not sufficient to overcome its lack of precision in capturing the sparse structure of the phase [Fig. 2(d)].

In conclusion, under the conditions of these simulations, $\xi - \alpha$NET demonstrated performance comparable to eLORETA in reconstructing the source log-spectrum and coherence, while significantly outperforming it in phase reconstruction. Notably, $\xi - \alpha$NET excelled in reconstructing sparse solutions. Additionally, $\xi - \alpha$NET operates at a fraction of the computational cost of eLORETA, making it especially advantageous for large-scale EEG source analyses where both speed and accuracy are critical.

Spatio-Temporal Distribution of Spectral Components

Bayesian Model Inversion of $\xi - \alpha$NET on the entire HarMNqEEG dataset also jointly estimates the source SCs of the EEG [Fig. 1(f)]. These SCs are parametrically modeled using the Student's t distributions that define the ξ and α processes in each voxel:

$$\begin{aligned} \boldsymbol{\xi}_i(\omega) &= t\big(\omega \mid \mathbf{e}_{i1}, \mathbf{e}_{i2}, \mathbf{e}_{i3}, 0\big), \\ \boldsymbol{\alpha}_i(\omega) &= t\big(\omega \mid \mathbf{a}_{i1}, \mathbf{a}_{i2}, \mathbf{a}_{i3}, \mathbf{a}_{i4}\big), \\ t(\omega \mid a, b, c, d) &= \frac{a}{\big(1 + b(\omega - d)^2\big)^c}, \end{aligned} \tag{4}$$

where $\mathbf{e} \in \mathbb{R}^{Nv \times 3}$ and $\mathbf{a} \in \mathbb{R}^{Nv \times 4}$ are the parameter matrices for the ξ and α processes, respectively, and i indexes voxels. In this formulation, $\mathbf{e}_{i1}$ and $\mathbf{a}_{i1}$ capture the power amplitudes of ξ and α at voxel i. They are sparse vectors because $\xi - \alpha$NET uses a Group Lasso prior across the rows of $\mathbf{e}$ and $\mathbf{a}$. To map the distribution of SCs across the Lifespan, we inverted $\xi - \alpha$NET on the entire HarMNqEEG, obtaining voxel-level power amplitudes $\mathbf{e}_{i,1}^{(j)}$ and $\mathbf{a}_{i,1}^{(j)}$ for each subject j. These values (see Supplementary Materials c) were then used to compute the probability of observing each SC in voxel i at age a by applying a Nadaraya–Watson Kernel Density Estimator:

$$\begin{aligned} f_\xi(i,a) &= \frac{1}{Z} \sum_{k,j=1}^{N_v, N_s} K_{\mathbf{H}}\big(a - a_j,\, l_{i,k}\big)\, \mathbb{I}\big(\mathbf{e}_{i,1}^{(j)} > T_\xi\big), \\ f_\alpha(i,a) &= \frac{1}{Z} \sum_{k,j=1}^{N_v, N_s} K_{\mathbf{H}}\big(a - a_j,\, l_{i,k}\big)\, \mathbb{I}\big(\mathbf{a}_{i,1}^{(j)} > T_\alpha\big), \\ Z(i,a) &= \sum_{k,j=1}^{N_v, N_s} K_{\mathbf{H}}\big(a - a_j,\, l_{i,k}\big), \\ K_{\mathbf{H}}(\mathbf{x}) &= \frac{9}{16} \prod_{k=1}^{2} \left(1 - \frac{x_k^2}{h_k^2}\right) \mathbb{I}\left(|x_k| < h_k\right), \end{aligned} \tag{5}$$

where $K_{\mathbf{H}}(\cdot)$ is the Epanechnikov kernel with a smoothing parameter $\mathbf{H} = \mathrm{diag}(h_1, h_2)$ selected by 10-fold cross-validation. Here, $l_{i,k}$ is the distance between voxels i and k, $Z(i,a)$ is a normalization constant, and $\mathbb{I}(\cdot)$ is an indicator function that equals one if the SC power exceeds a threshold (T_ξ or T_α).These thresholds are set automat-

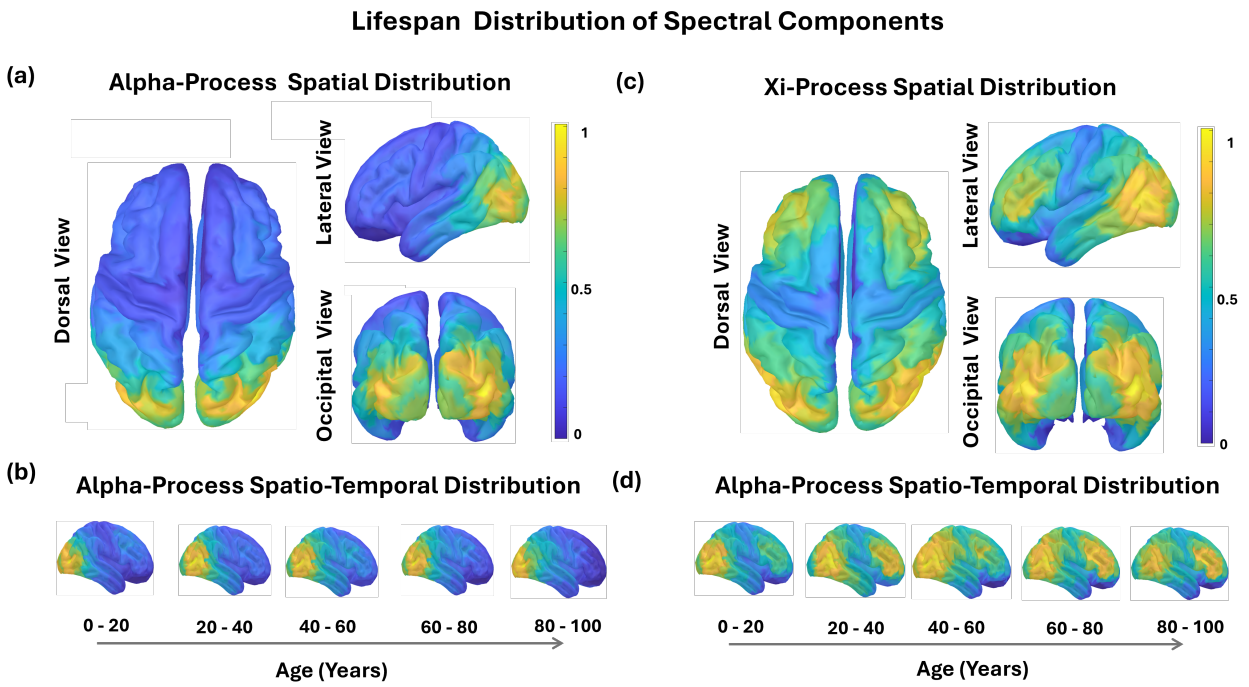

Figure 3. Lifespan Distribution of Spectral Components. Every voxel shows the probability of finding an active one of the spectral processes. (**a**) Shows the Alpha Process (spectral peak in the α-band) spatial distribution estimated from $\xi - \alpha$NET using model inversion on the HarMNqEEG dataset (Ns = 1965) at a resolution of Nv = 8003 voxels. As shown, the Alpha process is distributed with high probability on the visual areas of the brain with a gradient to lower values on the frontal areas. This indicates that the generators of the α-rhythms are spatially localized on the visual areas. (**b**) Shows the spatiotemporal distribution of the Alpha process across the Lifespan; we can observe that the areas of high probability shit from lower to higher order visual areas and back (**c**) Shows the spatial distribution of the generators of the Xi-Process (Aperiodic Component or Fractal Component of the EEG spectrum); in contrast, this spectral process encompasses all the areas of the brain, which suggests that this process has an isotropic spatial distribution on the cortical surface. (**d**) Across the Lifespan, the Xi Process generally has an isotropic distribution on the cortical surface, and the probability increases on the frontal areas with maturation.

ically by fitting a mixture of two Gaussian distributions on the power of the SC through the use of Expectation Maximization, and it is defined as the point at which the two Gaussian overlap (see details in Supplementary Material D). From the density estimation Eqs. (5), we compute the spatial distribution of Spectral Components as the marginal distribution across the age. It is important to note that the Nadaraya–Watson density estimator is known to be consistent and exhibits asymptotic normality under suitable regularity conditions. This ensures that, as the sample size grows, the estimator converges to the true underlying density, and its estimation error follows a normal distribution in the limit [34–36].

The results of conducting this analysis on the HarMNqEEG dataset can be appreciated in [Fig. 3]. That shows the Lifespan Distribution of SC. As we can appreciate, the α-Process or spectral peak on the α-band is localized with high probability on the occipital lobes but undergoes a small variation of the topological distribution across the Lifespan that shifts the areas of high probability from the visual areas V1 to higher order visual areas on V2, V3 and V4 and back as the subject maturates [Fig. 3(a)(b)]. This finding indicates that the generators of the α-rythms are localized in the visual areas. On the other hand, the generators of the ξ-process or AC can be described as an isotropic process on the cortical surface across the Lifespan [Fig. 3(c)(d)].These findings contrast with previously established conclusions performed by Valdes-Sosa et al. [17], Pascual et al. [8,18], Bosh et al., [37], Donoghue et.al. [9], that were conducted on small dataset of roughly hundreds. Our findings confirm these regularities on the basis of higher statistical power and spatial resolution.

Lifespan Trajectory of the Peak Alpha Frequency

The Peak Alpha Frequency (PAF) represents the specific frequency within the α-band (7–13 Hz) where the EEG power spectrum attains its maximum. Therefore, the PAF characterizes the mode frequency of the α-rythms. Although previous work has established age-related shifts in the scalp-level PAF [24,37–39], the source-space dynamics of these shifts, especially at high spatial resolution and with adequate statistical power, remain poorly understood.

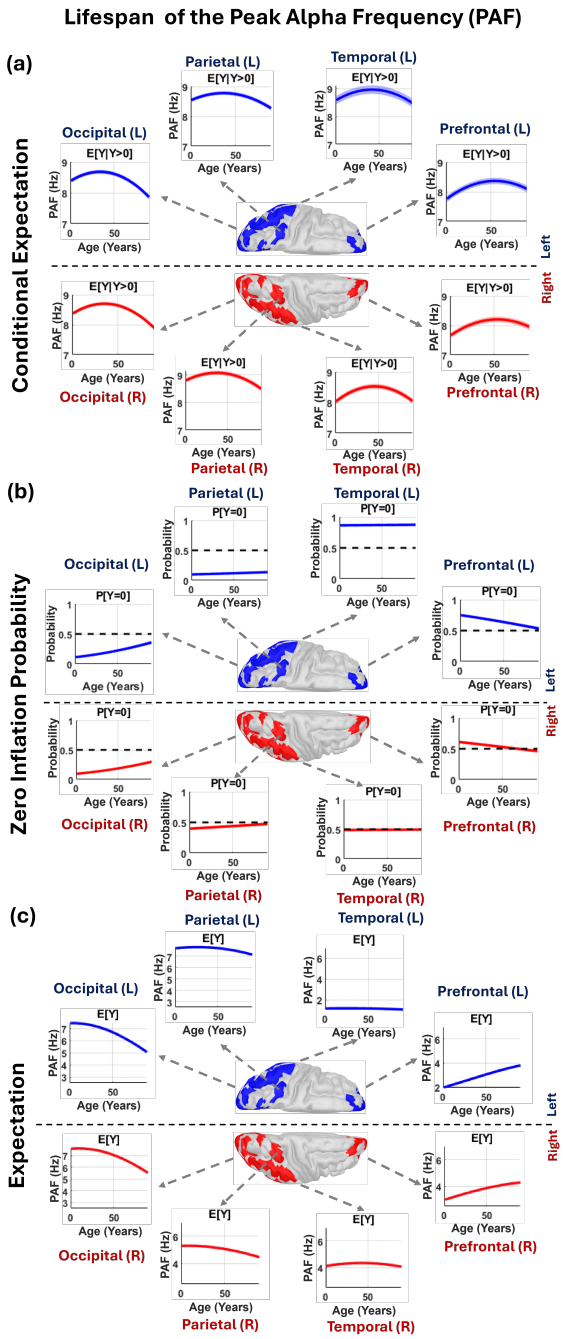

Figure 4. Lifespan trajectories of Peak Alpha Frequency (PAF). (**a**) The positive component of the PAF across all regions of interest (ROIs) and hemispheres follows an inverted U-shaped trajectory throughout the Lifespan, peaking near maturation age. (**b**) The probability of observing structural zeros (P[Y=0]) is not uniform across ROIs, showing a gradient of increasing zero-inflation probability from the occipital to the frontal lobes. This gradient, reported here for the first time, impacts the expected value of PAF and suggests structural variability in brain dynamics across regions. (**c**) The expected value of the PAF, incorporating the effects of structural zeros, shows a progressive flattening in its lifespan trajectory from the occipital to the frontal lobes.

Within the $\xi - \alpha$NET framework applied to HarMNqEEG, the PAF for subject j in voxel i is given by the parameter $\mathbf{a}^j_{i,4}$. Mapping these parameters against age, however, is not straightforward: $\xi - \alpha$NET enforces a Group Lasso prior across the rows of $\mathbf{e}^j$ and $\mathbf{a}^j$, producing a zero-inflated distribution of PAF estimates that violates the assumptions of standard linear regression. Consequently, we modeled the data using a Zero Inflated Gaussian (ZIG) model to account for zero inflation, positivity, and the band-limited nature of PAF [40–42].

We focused on a set of primary ROIs (r) in occipital, parietal, temporal, and prefrontal lobes across both hemispheres (listed in Supplementary Materials E). The ZIG used is

$$\begin{aligned} Y_{rij} &\sim \text{ZIG}\left(\mu_{rj}, \sigma^2_{rj}, \pi_{rj}\right), \\ \mu_{rj} &= \beta_0 + \beta_1 a_j + \beta_2 a_j^2 + \epsilon^{(1)}_{rj}, \\ \text{logit}\left(\pi_{rj}\right) &= \gamma_0 + \gamma_1 a_j + \epsilon^{(2)}_{rj}, \end{aligned} \tag{6}$$

where Y_{rij} is the PAF in ROI r for subject j, a_j is the subject's age, $\epsilon^{(\cdot)}_{rj}$ are random effects capturing voxel-level variability within each ROI and logit its the logit function ($\text{logit}(p) = \log\left(p/(1-p)\right)$). We fitted these ZIG models using the `glmmTMB` library in `R`. Here, π_{rj} denotes the probability of zero inflation, μ_{rj} is the expected value of the positive part of the distribution, and $\left(1-\pi_{rj}\right)\mu_{rj}$ gives the overall expected PAF.

Fig. 4 shows the outcome of applying ZIG regression to the PAF estimates of $\xi - \alpha$NET across the Lifespan. The positive portion (structural nonzeros) of the PAF data for all ROIs in both hemispheres follows an inverted U-shaped trajectory, peaking around middle age [Fig. 4(a)]. On the other hand, Zero-Inflation Probabilities are not uniformly distributed: they increase from occipital toward frontal regions. We can also see that for the ROIs on the temporal and Frontal lobes, the probability is above random ($p > 0.5$). To our knowledge, this is the first documented spatial gradient of zero inflation in PAF across the cortex, and it has a pronounced flattening effect on the expected PAF in frontal areas [Fig. 4(c)].

These findings are significant for three reasons. They confirm, with high spatial resolution and large sample size, the classic inverted U-shaped lifespan trajectory of PAF in source space reported on the literature [24,37–39]. Also, they demonstrate that PAF trajectories are not homogeneous across the cortex; rather, a zero-inflation gradient from posterior to frontal areas influences the shape of the developmental curves. Finally, our findings reveal that PAF trends are similar across hemispheres but can diverge by region once structural zeros are considered.

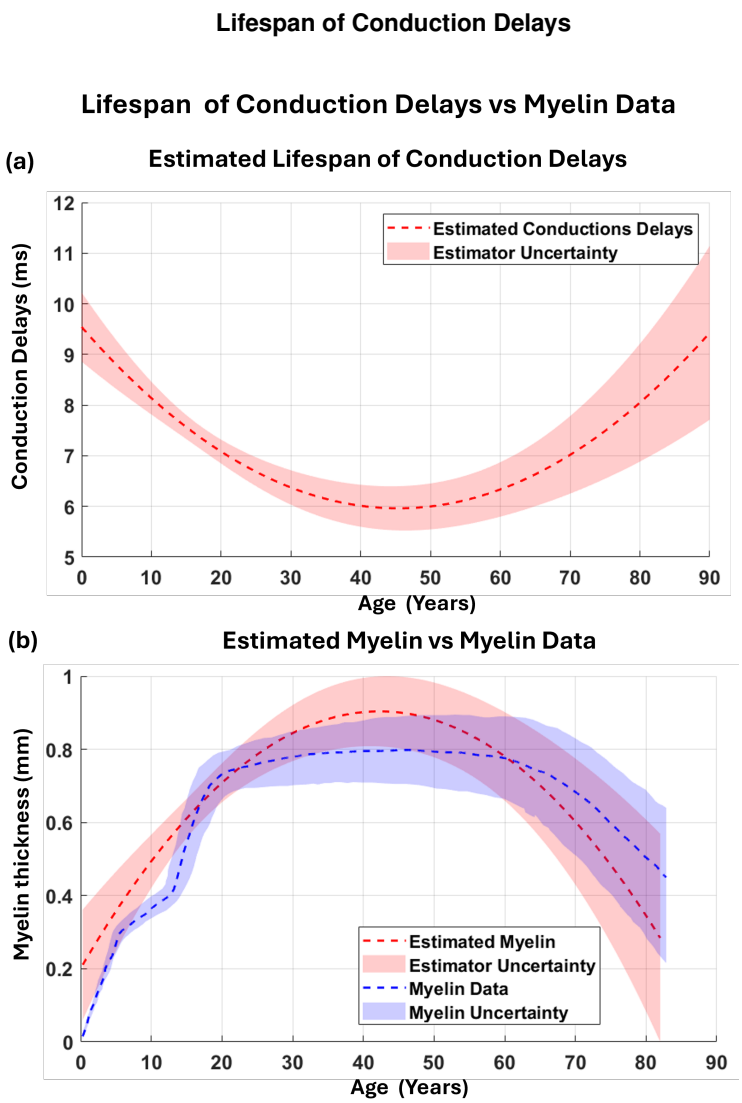

Figure 5. Lifespan of Conduction Delays vs Myelin Data. (**a**) Represent the Lifespan trajectory of conduction delays estimated using robust quadratic fit on estimated conduction delays of Ns= 1965 subjects of the HarMNqEEG using the Bayesian Model Inversion of the $\xi - \alpha$NET model. The regression reveals that the estimate follows a U-shape trajectory. (**a**) The estimated delays are mapped into myelin thickness, and then a robust quadratic fit is performed to reveal the Lifespan trajectory of estimated myelin thickness (red). When compared with independent myelin data, the regression shows that both quantities follow a similar qualitative inverted U-shape trajectory across the Lifespan with a peak between 40-50 years.

Conduction delays refer to the time it takes for an action potential to travel along neural tracts. These delays depend primarily on axon diameter and myelin thickness, both of which govern the speed of action potential propagation. Myelination is the process by which lipid-rich sheaths wrap axons (myelin thickness increases). This process produces an increase in the speed of transmission of action potential. As diffusion Magnetic Resonance Imaging (dMRI) studies show, myelin expression is not a static structure established early in development; rather, it changes throughout the Lifespan. Myelin thickness increases from childhood to adulthood, reaching a plateau before starting to decrease with maturation. Consequently, myelin expression follows an inverted U-shaped trajectory across the Lifespan, modulating conduction velocities and neural dynamics. [43–45]. According to the Rushton model [46], myelin thickness (d_m) is inversely proportional to the square of the average conduction delay ($\langle\tau\rangle$):

$$d_m \propto 1/\langle\tau\rangle^2. \tag{7}$$

Hence, the Rushton model and the trajectory of myelin thickness obtained using dMRI suggest that conduction delays should follow a U-shaped trajectory across the Lifespan. Nevertheless, these results have never been stated from EEG using a Structural Connectivity Model (SCM). To obtain the trajectory of conduction delays across the Lifespan, our starting point is the F-TRACT atlas, which provides the matrix representing the average conduction delays for the age group > 15, as provided by Lemarechal et al. [30] [Fig. 1(a)]. This data informs the generative model of the $\xi - \alpha$NET [Fig. 1(c)]. Specifically, subject-specific conduction delays $\boldsymbol{\tau}^{(j)}$ are estimated as:

$$\boldsymbol{\tau}^{(j)} = \mathbf{W}_D^{(j)} \odot \mathbf{D}, \tag{8}$$

where $\odot$ denotes the Hadamard element-wise product, $\mathbf{D} \in \mathbb{R}^{N_v \times N_v}$ is the baseline conduction-delay matrix from F-TRACT, and $\mathbf{W}_D^{(j)} \in \mathbb{R}^{N_v \times N_v}$ is a weight matrix that modulates $\mathbf{D}$ to reflect specific factors for subject j as they age. This weight matrix does not generally need to be symmetric and may represent a form of effective connectivity. However, the implications of these ideas are not explored in this paper. To simplify, we approximate the weight matrix as a scalar, $\mathbf{W}_D^{(j)} \rightarrow w_D^{(j)}$, thereby reducing the computational complexity involved in its estimation. The weight $w_D^{(j)}$ is then constrained within a reasonable search space by the following condition:

$$|w_D^{(j)} - 1| < \frac{\Delta_\tau}{\mu_\tau}, \tag{9}$$

where $\Delta_\tau = 5.5$ ms and $\mu_\tau = 9.5$ ms denote the Median Absolute Deviation and the Median of the conduction delays, respectively, as reported by Lemarechal et al. [30].

The Bayesian Model Inversion of the $\xi - \alpha$NET on the complete HarMNqEEG dataset [Fig. 1(e)(f)] yields $w_D^{(j)}$ for each subject. The average conduction delay $\langle\boldsymbol{\tau}^{(j)}\rangle$ is then computed as:

$$\langle\boldsymbol{\tau}^{(j)}\rangle = w_D^{(j)} \mu_\tau. \tag{10}$$

Using these estimates, we perform robust quadratic regression with age (a_j) as the covariate. As shown in [Fig. 5(a)], the conduction delays follow a U-shaped trajectory across the Lifespan, as theoretically predicted by the Rushton model. Specifically, the conduction delays decrease from childhood to adulthood, reaching a minimum of around 40 years, and then increase again with maturation. In [Fig. 5(b)], we qualitatively benchmark the estimated conduction delays by mapping them to myelin thickness (which is inversely proportional to the square of the average conduction delay) and comparing with independently reported myelin thickness trajectory by DeFaria et al. [43]. The results show that both the estimated myelin thickness and the myelin data follow a similar inverted U-shape trajectory across the Lifespan, peaking at the maturation age. Thus, these findings suggest that the Bayesian Inversion of the $\xi - \alpha$NET model can be used to map conduction delays from EEG data and that these delays follow a trajectory across the Lifespan that aligns closely with myelin data, supporting the utility of this approach for studying age-related neurophysiological changes.

CONCLUSION AND DISCUSSION

In neuroscience, traditional SCMs in source space typically follow a two-step, data-driven approach: first, an ESI method localizes brain activation, and then a spectral model fits the corresponding power spectrum. However, these models often neglect structural factors such as anatomical connectivity and conduction delays, which critically influence the spatiotemporal dynamics of neural oscillations. This oversight limits our understanding of the full range of source-level EEG SCs [9,17,24,37,47].

This paper introduces the $\xi - \alpha$NET model, which integrates structural connectivity and conduction delays into SCMs. By mapping SC dynamics across large datasets—such as the HarMNqEEG cross-spectrum dataset, with data from 1,965 subjects—the $\xi - \alpha$NET overcomes the computational limitations of traditional models, providing high spatial and statistical resolution. This approach enables the analysis of extensive datasets previously too complex to process.

Simulation benchmarks demonstrate that $\xi - \alpha$NET reconstructs source activations with similar accuracy to conventional methods, particularly in reconstructing source spectra and coherence matrices [Fig. 2]. Notably, the model significantly improves the reconstruction of coherence, a result attributed to its ability to capture optimal causal relationships embedded in conduction delays within brain networks [21, 22]. This feature is crucial for understanding the dynamic coupling between brain regions, where conduction delays reflect signal propagation times through the brain's white matter pathways.

A key finding is that the $\xi - \alpha$NET model enables the mapping of subject-specific conduction delays, revealing a U-shaped trajectory of delays across the Lifespan. Delays decrease during childhood, reach a minimum during maturation, and then increase again in adulthood. These findings align with established reports on myelination trajectories [43–45], providing new insights into how Myelination influences neural conduction at the network level [Fig. 5]. Although we estimate a global average conduction delay in this study, the $\xi - \alpha$NET model can be extended to map subject-specific conduction delays across all brain tracts, offering a more accurate representation of effective connectivity between neural generators. This capability is particularly important for normative studies of conduction delays, which are essential for age- and subject-specific neural field simulations, with clinical applications in disease diagnosis, such as epilepsy [20,48], and the creation of personalized "digital twin" models. An interesting connection exists between detailed modeling, as in [19,25–28], and our work. On the one hand, our approach provides large-scale constraints that must be satisfied by any more detailed model. On the other, more realistic models could help uncover the underlying mechanisms behind the macroscopic regularities we have described.

We also mapped the spatiotemporal distribution of α-rhythm and fractal invariant activity (α and ξ processes) using Kernel Density Estimation (KDE). Our findings show that α-rhythm generators are localized to visual regions of the brain, with a topological shift from lower to higher-order visual areas across the Lifespan. In contrast, the fractal ξ-process is isotropically distributed across the cortical surface, with a childhood gradient localized to the occipital lobes that disperse with maturation [Fig. 3]. These findings confirm preivious research on the basis of high statistical power and spatial resolution [8,9,17,18,37,47].

Furthermore, we found that the mode frequency that characterizes the α-rythms, i.e., PAF, follows an inverted U-shape trajectory across the Lifespan. This was possible by the use of Zero Inflated regression Model on the SC parameters estimated inverting the $\xi - \alpha$NET on the HarM-

NqEEG data set. Additionally, we were able to map the Zero Inflated Probability of the PAF, where we were able to document for the first time a spatial gradient of zero inflation across the cortex from the occipital to frontal lobes, indicating a flattening in the variability of the Lifespan, the trajectory of the expected PAF to the frontal lobes of the brain [Fig. 4]. These results align and expand the previous findings in the literature [37,38].

Despite its strengths, the $\xi-\alpha$NET model has several limitations. The simplification of thalamocortical dynamics into a Multivariate Autoregressive (MVAR) model, while computationally efficient, does not account for the full excitatory-inhibitory balance that shapes network dynamics. Moreover, the model assumes that network dynamics are driven solely by causal relationships between oscillatory generators, neglecting feedback mechanisms and bidirectional influences between regions, which are critical to understanding the true complexity of brain networks. Additionally, the Dirac delta distribution used to model conduction delays simplifies the delay structure, which may be more complex and heterogeneous across different brain regions. Furthermore, the focus on two SC—the ξ process or AC and α spectral peak —limits the model's ability to capture other important oscillatory components such as theta, beta, and gamma rhythms. While the model could be extended to include these components, the decision to focus on just two was made for simplicity in this work. Finally, while Bayesian inference is a powerful tool for estimating model parameters, the constrained search space limits the model's ability to explore all possible solutions. Expanding the search space could improve the model's flexibility and accuracy, particularly in representing the full complexity of neural oscillations.

In summary, the $\xi-\alpha$NET model represents an advancement in EEG SCMs, providing new insights into neural oscillations and their underlying network dynamics. The model's ability to integrate structural connectivity, conduction delays, and high-resolution spectral dynamics opens up new avenues for normative studies, as well as clinical applications such as personalized brain modeling for disease diagnosis and treatment. Future work could address the model's limitations by incorporating more complex network dynamics and additional SCs.

MATERIALS AND METHODS

Resources and Code

All numerical computations and simulations were performed on a high-performance server equipped with 52 CPUs and 256 GB of RAM. The $\xi-\alpha$NET parameter estimation algorithm, along with a visual interface for analysis and visualization, is available upon request on GitHub https://github.com/CCC-members

Data

Two types of data were used: structural data for informing the $\xi-\alpha$NET model and empirical data for analysis. For the structural data, we used the anatomical connectivity matrix $\mathbf{C}$ from Rosen et al. [49], which was derived from diffusion MRI (dMRI) to estimate axonal fibers linking cortical areas. These estimates were calibrated using histological measurements of callosal fiber density and are available via the HCP-MNP1.0 parcellation. Axonal conduction delays $\mathbf{D}$ were obtained from the F-TRACTS consortium, based on data from 780 epilepsy patients [30]. These delays were preprocessed using Gaussian process regression and integrated with neurotract length $\mathbf{L}$ [49] (see Supplementary Materials F). Both anatomical and conduction delay data were mapped from ROI space to voxel space. The head model, source model, and lead field matrix ($\mathbf{K}$) were derived using the Ciftistorm pipeline, applying the HCP-MNP1.0 anatomy template [50].

Empirical data were sourced from the HarM-NqEEG dataset, which includes scalp EEG cross-spectral tensors from 1,965 subjects across nine countries. The dataset covers multiple age groups and was acquired using various devices. Each tensor has dimensions $N_c \times N_c \times N_w$, where $N_c = 19$ EEG channels and $N_w = 47$ frequency bins. Preprocessing steps, as detailed in [24], included applying an average reference, removing the global scaling factor, and ensuring the positive definiteness of the cross-spectral matrices. Visualization outputs were generated using the functions included in the BC-VARETA toolbox [51].

FUNDING

This research was funded by the grant Y0301902610100201 of the University of Electronic Sciences and Technology of China UESTC and the Chengdu Science and Technology Bureau Program under Grant 2022-GH02-00042- HZ. LM gratefully acknowledges

the support of the" Hundred Talents" program of the University of Electronic Science and Technology of China.

REFERENCES

1. Engel AK, Fries P and Singer W. Dynamic predictions: oscillations and synchrony in top–down processing. *Nature Reviews Neuroscience* 2001; **2**: 704–716.
2. Buzsaki G and Draguhn A. Neuronal oscillations in cortical networks. *science* 2004; **304**: 1926–1929.
3. Miller KJ, Sorensen LB, Ojemann JG *et al.* Power-law scaling in the brain surface electric potential ; **5**: e1000609.
4. He BJ. Scale-free brain activity: past, present and future ; **18**: 480–487.
5. Cáceres JLH, Comas LD, Cordovés JMA *et al.* Assessing Ibico, a bicoherence-derived multi-frequency index measured from eeg signals. *Revista Cubana de Informática Médica* 2024; **16**: 721.
6. Reyes RG and Martinez Montes E. Modeling neural activity in neurodegenerative diseases through a neural field model with variable density of neurons. *bioRxiv* 2022; 2022–08.
7. Nechipurenko YD, Reyes RG and Caceres JH. Hypothesis on pollution of neuronal membranes, epilepsy and ketogenic diet. *Biophysics* 2021; **66**: 956–964.
8. Pascual-marqui RD, Valdes-sosa PA and Alvarez-amador A. A parametric model for multichannel EEG spectra ; **40**: 89–99.
9. Donoghue T, Haller M, Peterson EJ *et al.* Parameterizing neural power spectra into periodic and aperiodic components. *Nature neuroscience* 2020; **23**: 1655–1665.
10. Zetterberg LH. Estimation of parameters for a linear difference equation with application to eeg analysis. *Mathematical Biosciences* 1969; **5**: 227–275.
11. Amador A, Valdés Sosa P, Pascual Marqui R *et al.* On the structure of EEG development ; **73**: 10–19.
12. Whitten TA, Hughes AM, Dickson CT *et al.* A better oscillation detection method robustly extracts eeg rhythms across brain state changes: the human alpha rhythm as a test case. *Neuroimage* 2011; **54**: 860–874.
13. Wen H and Liu Z. Separating fractal and oscillatory components in the power spectrum of neurophysiological signal. *Brain topography* 2016; **29**: 13–26.
14. Wilson LE, da Silva Castanheira J and Baillet S. Time-resolved parameterization of aperiodic and periodic brain activity. *Elife* 2022; **11**: e77348.
15. Brady B and Bardouille T. Periodic/aperiodic parameterization of transient oscillations (papto)–implications for healthy ageing. *NeuroImage* 2022; **251**: 118974.
16. Hu S, Zhang Z, Zhang X *et al.* xi-pi: A nonparametric model for neural power spectra decomposition ; **28**: 2624–2635. Conference Name: IEEE Journal of Biomedical and Health Informatics.
17. Valdés P, Bosch J, Grave R *et al.* Frequency domain models of the eeg. *Brain topography* 1992; **4**: 309–319.
18. Pascual-Marqui RD, Kochi K and Kinoshita T. Cortical xi-alpha model for resting state electric neuronal activity. *arXiv preprint arXiv:2212.13571* 2022; .
19. Feng J, Jirsa V and Lu W. Human brain computing and brain-inspired intelligence 2024.
20. Wang HE, Triebkorn P, Breyton M *et al.* Virtual brain twins: from basic neuroscience to clinical use. *National Science Review* 2024; **11**: nwae079.
21. Nolte G, Ziehe A, Nikulin VV *et al.* Robustly estimating the flow direction of information in complex physical systems ; **100**: 234101.
22. Nolte G, Meinecke FC, Ziehe A *et al.* Identifying interactions in mixed and noisy complex systems ; **73**: 051913. Publisher: American Physical Society.
23. Reyes RG and Valdes-Sosa PA. Mapping effective connectivity 2025; .
24. Li M, Wang Y, Lopez-Naranjo C *et al.* Harmonized-multinational qeeg norms (harmnqeeg). *NeuroImage* 2022; **256**: 119190.
25. Feng J. Simulating the whole brain as an alternative way to achieve agi. *Quantitative Biology* 2023; **11**: 471–473.
26. Li Y, Li X, Shen S *et al.* Dtbvis: An interactive visual comparison system for digital twin brain and human brain. *Visual Informatics* 2023; **7**: 41–53.
27. Lu W, Zeng L, Du X *et al.* Digital twin brain: a simulation and assimilation platform for whole human brain. *arXiv preprint arXiv:2308.01241* 2023; .
28. Lu W, Zeng L, Wang J *et al.* Imitating and exploring the human brain's resting and task-performing states via brain computing: scaling and architecture. *National Science Review* 2024; **11**: nwae080.
29. Friedman J, Hastie T and Tibshirani R. A note on the group lasso and a sparse group lasso. *arXiv preprint arXiv:1001.0736* 2010; .
30. Lemaréchal JD, Jedynak M, Trebaul L *et al.* A brain atlas of axonal and synaptic delays based on modelling of cortico-cortical evoked potentials ; **145**: 1653–1667.
31. Pascual-Marqui RD, Lehmann D, Koukkou M *et al.* Assessing interactions in the brain with exact low-resolution electromagnetic tomography. *Philosophical Transactions of the Royal Society A: Mathematical, Physical and Engineering Sciences* 2011; **369**: 3768–3784.
32. Van Veen BD, Van Drongelen W, Yuchtman M *et al.* Localization of brain electrical activity via linearly constrained minimum variance spatial filtering. *IEEE Transactions on biomedical engineering* 1997; **44**: 867–880.
33. Hämäläinen MS and Ilmoniemi RJ. Interpreting magnetic fields of the brain: minimum norm estimates. *Medical & biological engineering & computing* 1994; **32**: 35–42.
34. Terrell GR and Scott DW. Variable kernel density estimation. *The Annals of Statistics* 1992; 1236–1265.
35. Ruppert D and Wand MP. Multivariate locally weighted least squares regression. *The annals of statistics* 1994; 1346–1370.
36. Fan J. *Local polynomial modelling and its applications: monographs on statistics and applied probability 66*, (Routledge2018).
37. Bosch-Bayard J, Valdés-Sosa P, Virues-Alba T *et al.* 3d statistical parametric mapping of eeg source spectra by means of variable resolution electromagnetic tomography (vareta). *Clinical Electroencephalography* 2001; **32**: 47–61.
38. Park J, Ho RL, Wang We *et al.* The effect of age on alpha rhythms in the human brain derived from source localized resting-state electroencephalography. *NeuroImage* 2024; **292**: 120614.

39. Turner C, Baylan S, Bracco M *et al.* Developmental changes in individual alpha frequency: Recording eeg data during public engagement events. *Imaging Neuroscience* 2023; **1**: 1–14.
40. Zuur AF, Ieno EN, Walker N *et al.* Zero-truncated and zero-inflated models for count data. *Mixed effects models and extensions in ecology with R* 2009; 261–293.
41. Zhang X, Guo B and Yi N. Zero-inflated gaussian mixed models for analyzing longitudinal microbiome data. *Plos one* 2020; **15**: e0242073.
42. Brooks ME, Kristensen K, van Benthem KJ *et al.* Modeling zero-inflated count data with glmmtmb. *BioRxiv* 2017; 132753.
43. de Faria Jr O, Pivonkova H, Varga B *et al.* Periods of synchronized myelin changes shape brain function and plasticity. *Nature Neuroscience* 2021; **24**: 1508–1521.
44. Dvorak AV, Swift-LaPointe T, Vavasour IM *et al.* An atlas for human brain myelin content throughout the adult life span. *Scientific reports* 2021; **11**: 269.
45. Newman BT, Jacokes Z, Venkadesh S *et al.* Conduction velocity, g-ratio, and extracellular water as microstructural characteristics of autism spectrum disorder. *Plos one* 2024; **19**: e0301964.
46. Rushton W. A theory of the effects of fibre size in medullated nerve. *The Journal of physiology* 1951; **115**: 101.
47. Valdés-Sosa PA, Sánchez-Bornot JM, Lage-Castellanos A *et al.* Estimating brain functional connectivity with sparse multivariate autoregression ; **360**: 969–981.
48. Mitjans AG, Linares DP, Naranjo CL *et al.* Accurate and efficient simulation of very high-dimensional neural mass models with distributed-delay connectome tensors. *NeuroImage* 2023; **274**: 120137.
49. Rosen BQ and Halgren E. An estimation of the absolute number of axons indicates that human cortical areas are sparsely connected ; **20**: e3001575.
50. Areces-Gonzalez A, Paz-Linares D, Riaz U *et al.* Ciftistorm pipeline: facilitating reproducible eeg/meg source connectomics. *Frontiers in Neuroscience* 2024; **18**: 1237245.
51. Paz-Linares D, Gonzalez-Moreira E, Areces-Gonzalez A *et al.* Minimizing the distortions in electrophysiological source imaging of cortical oscillatory activity via spectral structured sparse bayesian learning ; **17**: 978527.